Nano Research
2023, 16(5): 6057–6066

ISSN 1998-0124 CN 11-5974/O4
https://doi.org/10.1007/s12274-022-4676-9

Research Article

Cobalt-iron oxide/black phosphorus nanosheet heterostructure: Electrosynthesis and performance of (photo-)electrocatalytic oxygen evolution

Man Zhao[1,§], Xiaoru Cheng[1,§], He Xiao[1] (✉), Jianru Gao[1], Shoufeng Xue[1], Xiaoxia Wang[1], Haishun Wu[1], Jianfeng Jia[1] (✉), and Nianjun Yang[2] (✉)

[1] *Key Laboratory of Magnetic Molecules & Magnetic Information Materials Ministry of Education, The School of Chemical and Material Science, Shanxi Normal University, Taiyuan 030000, China*
[2] *Institute of Materials Engineering, University of Siegen, Siegen 57076, Germany*
[§] *Man Zhao and Xiaoru Cheng contributed equally to this work.*

Received: 5 April 2022 / **Revised:** 26 May 2022 / **Accepted:** 18 June 2022

ABSTRACT

Highly active, stable, and cut-price (photo-)electrocatalysts are desired to overwhelm high energy barriers for anodic oxygen evolution reaction processes. Herein, a heterostructure of cobalt-iron oxide/black phosphorus nanosheets is *in-situ* synthesized via a facile and novel three-electrode electrolysis method. Bulky black phosphorus is exfoliated into its nanosheets at the cathode while the CoFe oxide is derived directly from the metal wire anode during the electrolysis process. This heterostructure exhibits excellent electrocatalytic oxygen evolution reaction (OER) performance, and the overpotential at 10 mA·cm^{-2} is 51 mV lower than that of the commercial RuO_2 catalyst. Its superior OER performance stems from the favorable adsorption behavior and an enlarged electrochemical active surface area of the catalyst. To reveal the origin of excellent OER performance from the point of adsorption strength of OH*, methanol oxidation reaction (MOR) test is applied under the identified OER operating conditions. Further introduction of light illumination enhances the OER activity of this heterostructure. The overpotential drops down to 280 mV, benefiting from pronounced photochemical response of black phosphorus nanosheets and iron oxide inside the heterostructure. This work develops a new electrochemical method to construct high performance and light-sensitive heterostructures from black phosphorus nanosheets for the OER.

KEYWORDS

electrosynthesis, oxygen evolution reaction, black phosphorus, cobalt oxide, iron oxide

1 Introduction

In recent years, plenty of works have been carried out to develop clean and efficient technologies for hydrogen production. Electrocatalytic hydrogen production via water splitting has been considered as one highly efficient and ecofriendly route. However, the anodic oxygen evolution reaction (OER), another half-reaction of water splitting, has sluggish kinetics, leading to high energy barriers that need to be overwhelmed during water splitting [1–5]. To reduce such energy barriers of the OER, noble Ir- or Ru-based electrocatalysts have been frequently utilized as the OER catalysts [6–9]. Nevertheless, the scarcity and high cost of these precious metals restrain their large-scale applications. Thus, the exploration of low-cost electrocatalysts for the OER with high activity and stability is urgently required.

Iron metal oxides have been widely applied as an economic and efficient electrocatalysts for the OER. It has been reported that their OER activity can be enhanced if multiple metal compounds such as coupling CoO_x or NiO_x into the metal oxide matrix are constructed [10–14]. This is because the interaction of multiple metal centers can efficiently regulate and optimize the electronic structure, charge-carrier density, and electron conductivity of those compounds [11, 15].

Meanwhile, black phosphorus (BP) has been employed as a latent OER (photo-)electrocatalyst. This is because this two-dimensional (2D) material features superior properties, including high carrier mobility, strong optical absorption, and tunable direct band gap [16–21]. Unfortunately, the applications of exfoliated black phosphorus nanosheets (BP NSs) are quite limited in that they are rapidly deteriorated in air and own unfavorable adsorption toward oxygen-containing intermediates. Note that the deterioration of BP NSs can be suppressed by the formation of their heterostructures with different metal compounds, such as the heterostructures of Co_3O_4/BP, Co_2P/BP, and CoFeO/BP [22–24]. These metal-based materials could passivate the defects of BP NSs. Furthermore, the coupling of BP NSs with some transition metal-based nanomaterials could adjust adsorption of the oxygen-containing intermediate [25]. Stemming from the electronic interactions between BP NSs and metal-based materials, an optimal electronic status of such a heterojunction was obtained, which in turn facilitated its OER performance. However, most studies focus on suppressing deterioration of BP NSs, and few

Address correspondence to He Xiao, xiaohe200808@sxnu.edu.cn; Jianfeng Jia, jiajf@dns.sxnu.edu.cn; Nianjun Yang, nianjun.yang@uni-siegen.de

works are concentrated on modulation of the adsorption oxygen-containing intermediates on these heterojunctions in detail.

In this work, cobalt-iron oxide is thus coupled with BP NSs. This hybrid material or this heterostructure is supposed to exhibit superior OER performance, due to the following reasons. Firstly, the electronic interaction between BP NSs and cobalt-iron oxide can optimize adsorption of the oxygen-containing intermediates to a superior status. Secondly, cobalt-iron oxides can offer many active sites for the OER and their homogeneous growth on BP NSs supporter is also expected, originating from the strong interactions between surface phosphorus atoms and metal cations. Note here that the supporter of BP NSs also serves as a charge transport medium to enhance charge conduction. Finally, the BP NSs and iron oxide in Co-Fe/BP have a favorable band gap structure. Their excellent optical absorption features can expand their photoelectrochemical applications, such as a photoelectrochemical catalyst for the OER. Moreover, the CoFe oxide/BP heterostructure was prepared by a simple and novel electrochemical method with a three-electrode system (single cathode-double anodes) in this study. Thanks to the contraption, two components are separately synthesized at the anode and the cathode during the electrolysis process. Namely, bulky black phosphorus is exfoliated into BP NSs at the cathode and simultaneously CoFe oxide is formed at the anode from their metal state. As-formed heterostructure is characterized using different techniques and further applied for the OER. The effect of its composition on the enhancement of the OER performance is investigated. The superior electrocatalytic OER activity to a noble RuO_2 catalyst is attributed to the synergistic effect between CoFe oxide and BP NSs, where favorable light adsorption and an enlarged electrochemical active surface area are realized.

2 Experimental

2.1 Chemicals and materials

Cobalt wire and iron wire were bought from Runde Metal Material Company (China). Bulky BP was bought from Kunming Black Phosphorous Company (China). Tetrabutylammonium tetrafluoroborate ($TBABF_4$, 98%) and propylene carbonate (PC, 99.9%) were bought from Aladdin.

2.2 Preparation of Co-Fe/BP heterostructures

A facile three-electrode method was designed to synthesize a CoFe oxide/BP NSs hybrid (Fig. 1). Both a cobalt wire and an iron wire served as the anode while 40 mg bulky BP was used as the cathode. These three electrodes were dipped in PC solvent containing 0.8 M $TBABF_4$. The work voltage was set as 30 V for several hours as needed. Subsequently, the BP was collected from the cathode and mixed with the electrolyte solvent. This mixed solution was finally transferred to an 80 mL Teflon-lined container. Under Ar atmosphere, the resultant suspension was stirred (500 rpm) and treated at 160 °C for 12 h. Finally, the solution was filtered. As-obtained product was washed with PC solution twice and ethanol twice, and dried at 60 °C for 8 h. An ink was prepared by dispersing 5.0 mg of an as-synthesized catalyst in a mixture of 0.75 mL of anhydrous ethanol, 0.25 mL of ultrapure water, and 0.03 mL of 5 wt.% Nafion solution ($TBABF_4$ was chosen as the electrolyte because of the large-sized TBA^+ cations. TBA^+ cations were triggered to insert into the interlayers of black phosphorus under electric field, resulting in the expansion, curling, stripping, and peeling of black phosphorus. PC solvent could not only dissolve the $TBABF_4$ electrolyte, and reduce the oxidation and degration of black phosphorus, but also insert the interlayer after entrance of TBA^+ and further promote the exfoliation degree of black phosphorous. Moreover, here the high voltage of 30 V was applied, because it was also in favor of enhancing exfoliation degree of bulky BP).

2.3 Materials characterization

X-ray diffraction (XRD) tests were conducted on an X-ray diffractometer (Ultima IV-185) with Cu Kα radiation. X-ray photoelectron spectroscopy (XPS, Thermo Fisher Scientific) was carried out using an Al Kα X-ray source. Transmission electron microscopy (TEM) and scanning electron microscopy (SEM) images were recorded using the FEI Tecnai F20 and JSM-7001F, respectively. The chemical compositions (Co and Fe) of these as-prepared materials were detected by inductively coupled plasma optical emission spectrometry (ICP-OES).

2.4 Electrochemical measurements

Electrochemical properties of these synthesized materials were investigated in 1 M KOH solution on a CHI 660E electrochemical workstation (CH Instruments, Inc., Shanghai, China). In some cases, light was illuminated. A graphite rod, Hg/HgO, and a glassy carbon electrode (GCE, 3 mm in diameter) were served as counter electrode, reference electrode, and working electrode, respectively. For the OER experiments, the catalyst ink (5 μL) was coated on the GCE. The overpotential was measured by means of linear sweep voltammetry, ranging from 0 to 1 V (vs. Hg/HgO) at a scan rate of 5 $mV \cdot s^{-1}$. Tafel plots were gained by redrawing related linear sweep voltammograms (LSVs) according to the Tafel equation. The electrochemical impedance spectroscopy (EIS) was carried out in a frequency range from 10^5 to 1 Hz at a current density 10 $mA \cdot cm^{-2}$. All potentials throughout the paper were converted to reversible hydrogen electrode (RHE) according to the equation of $E_{RHE} = E_{Hg/HgO} + 0.059\ pH + E^{\theta}_{Hg/HgO}$.

3 Results and discussion

3.1 Characterization of Co-Fe/BP heterostructures

During the synthesis of CoFe oxide/BP heterostructure, the application of an operation voltage of 30 V for 4 h in PC + 0.8 M

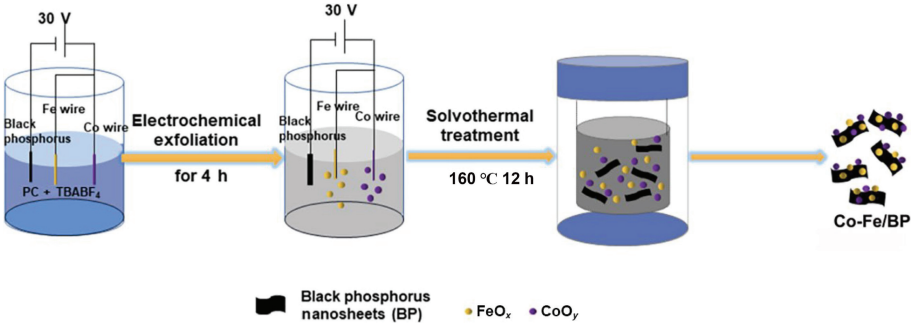

Figure 1 Schematic steps of electrosynthesis of Co-Fe/BP heterostructures.

$TBABF_4$ leads to the expansion of bulky BP, due to the insertion of large-sized TBA^+ cations. The bulky BP is then exfoliated into nanosheets at the cathode, which are expected to feature a high carrier mobility and abundant active edge sites. At the anode, both cobalt wire and iron wire are oxidized, generating cobalt ions and iron ions in the solution. The treatment of such a mixture using a solvothermal approach and a subsequent calcination process results in the preparation of the heterostructures of cobalt-iron oxide and BP NSs, defined as Co-Fe/BP in this paper. Benefiting from the reductive electrolyte solution under electrolysis condition [26, 27], a low-crystallinity metal oxidation structure is more easily to be formed. Such low-crystallinity structure can provide more active sites for OER and in turn enhance the electrocatalytic activity ofthis heterostructure. For comparison, electrocatalysts made from only cobalt or iron were also synthesized, which are defined as Co/BP or Fe/BP, respectively. This designed three-electrode electrolysis method shows two advantages: For the one, the preparation process is very simple and the hybrid is more easily obtained. The exfoliation process of bulky BP into BP nanosheets is coupled with the preparation process of Co-Fe oxide, which simplifies the traditionally individual synthesis processes; for the other, this method facilitates the formation of low-crystallinity Co-Fe oxide with more active sites due to the influence of the electrolyte solution under electrolysis condition, which avoids the precursors of metal salts.

The phases of these electrocatalysts were verified by means of XRD. The XRD patterns (Fig. S1 in the Electronic Supplementary Material (ESM)) of BP, Co/BP, Fe/BP, and Co-Fe/BP samples all show three main characteristic peaks located at 16.9°, 34.1°, and 52.3°, which can be assigned to the (020), (040), and (060) planes of BP, respectively. Due to the high intensity of these three peaks, other peaks are almost invisible for BP from Fig. S1 in the ESM. With the introduction of Co or Fe to BP, the intensity of three peaks decreases substantially, thus these original small peaks are highlighted. To observe them clearly, the spectra of XRD are amplified (Fig 2(a)). These apparent peaks at 26.4°, 35.0°, 40.1°, 55.8°, and 56.7° are assigned to (021), (111), (041), (200), and (132) of BP (PDF#73-1358), respectively. For Fe/BP, a new peak

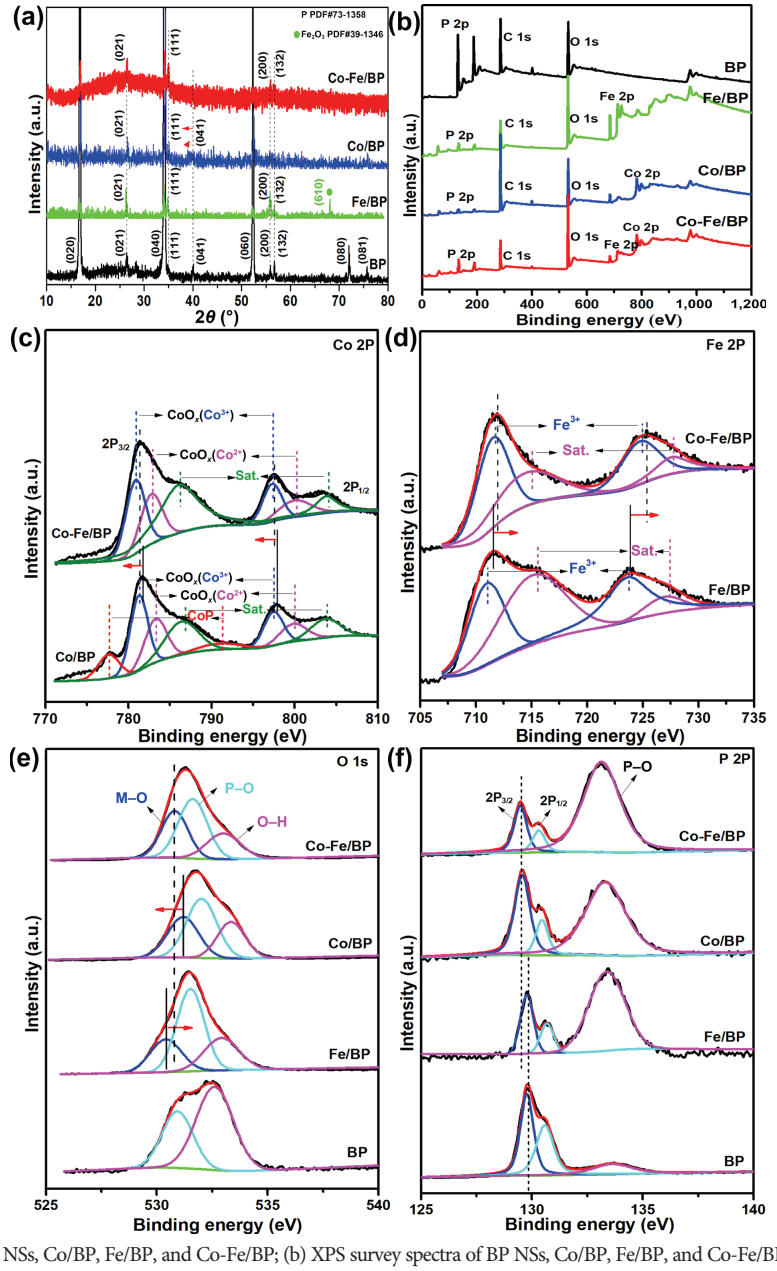

Figure 2 (a) XRD patterns of BP NSs, Co/BP, Fe/BP, and Co-Fe/BP; (b) XPS survey spectra of BP NSs, Co/BP, Fe/BP, and Co-Fe/BP; (c) Co 2p XPS spectra of Co/BP and Co-Fe/BP; (d) Fe 2p XPS spectra of Fe/BP and Co-Fe/BP; (e) O 1s XPS spectra of BP NSs, Co/BP, Fe/BP, and Co-Fe/BP; and (f) P 2p XPS spectra of BP NSs, Co/BP, Fe/BP, and Co-Fe/BP.

shows up, which is located at 68.2° and corresponded to (610) plane of Fe_2O_3 (PDF#39-1348). This indicates the formation of Fe_2O_3 on Fe/BP. Moreover, for Co/BP, it is observed that (041) peak shifts slightly to a small angle compared with BP. This shift results from an enlarged interlayer space of BP due to the doping of the Co species, which is consistent with previous work [16]. Namely, single cobalt or iron species could be formed on the BP NSs [28]. However, with coloading of Co and Fe species on BP, the obtained Co-Fe/BP does not show the characteristic peaks of Co and Fe species, suggesting the crystallinity of formed Co species and Fe species is extremely low.

The surface valence states of these catalysts were probed by XPS. Their XPS survey spectra indicate the presence of cobalt or/and iron, phosphorus, carbon, and oxygen species (Fig. 2(b)). This is further verified by their ICP-OES results (Table S1 in the ESM). In their high-resolution Co 2p XPS spectra (Fig. 2(c)), the Co/BP catalyst shows two small peaks that are located at 777.8 and 792.3 eV. Both of them correspond to Co 2p in Co_xP (Co^{0+}) [24]. In addition, two peaks arising at 781.3 and 797.6 eV are ascribed to CoO_x (Co^{3+}) species, while those at 786.8 and 803.9 eV are attributed to the CoO_x (Co^{2+}) species. Therefore, the formation of Co_xP and CoO_x over the BP NSs is confirmed. With the introduction of Fe, the peaks that are assigned to the Co_xP species disappear, suggesting that the incorporation of Fe affects the chemical states of Co. Moreover, a negative shift of the binding energy (BE) by about 0.4–0.5 eV in the Co region for Co-Fe/BP is observed relative to Co/BP, meaning with the introduction of Fe, more electrons transfer to Co species. In the Fe 2p XPS spectra, the peak fitting analysis suggests that iron in Fe/BP serves as Fe^{3+}, with two fitted peaks at 711.2 and 723.7 eV, assigned to Fe $2p_{3/2}$ and Fe $2p_{1/2}$, respectively (Fig. 2(d)). This indicates that Fe_2O_3 is formed over Fe/BP. Meanwhile, it is noticed that the whole Fe 2p peaks over Co-Fe/BP show a positive shift (0.45–1.4 eV) in comparison with that over Fe/BP, indicating the electrons migrate away from the Fe species.

The peaks in the O 1s XPS spectra of these catalysts (Fig. 2(e)) were deconvoluted into two peaks: one peak at 532.9 eV that is assigned to OH and another at 530.9 eV that corresponds to a P–O bond. In addition to these OH and P–O groups, the Co/BP, Fe/BP, and Co-Fe/BP catalysts exhibit a new peak, which is associated with an oxygen–metals (O–M) group in comparison with BP NSs. Consequently, metal oxides are presented in these catalysts/heterostructures. This fitted O–M peak (530.8 eV) in Co-Fe/BP is just present at the medium position between Fe/BP (530.4 eV) and Co/BP (531.2 eV). Combining O 1s XPS spectra with Co 2p XPS spectra as well as Fe 2p XPS spectra, it is concluded that Co-O-Fe interfacial species are generated. Electron migration from Fe to Co along the way of O bridge via the interface could effectively regulate the electronic structure, which in turn optimizes the adsorption and enhances electrochemical behavior of Co-Fe/BP [29, 30].

The high-resolution P 2p XPS spectra of these catalysts were also recorded, including BP NSs as well as the Co/BP, Fe/BP, and Co-Fe/BP catalysts (Fig. 2(f)). For BP NSs, three peaks are present at 129.8, 130.5, and 133.7 eV, which are assigned to P $2p_{3/2}$, P$2p_{1/2}$, and P–O, respectively. While the binding energies of P 2p in the Co/BP, Fe/BP, and Co-Fe/BP catalysts are shifted toward lower binder energies when compared with that of BP NSs. In this context, strong electron interactions between Co (or Fe) and BP exist. This phenomenon also indicates that these generated Co/BP, Fe/BP, and Co-Fe/BP catalysts are heterostructures, not simple mixtures.

To examine the surface properties of these catalysts, their Raman spectra were recorded (Fig. 3). In the Raman spectrum of BP NSs, three vibrational bands arise at approximately 359.2 cm^{-1}, 434.4 cm^{-1}, and 462.5 cm^{-1}, which can be assigned to the out-of-plane A_g^1 mode, in-plane B_{2g}, and A_g^2 vibration modes of BP, respectively [22]. While these three peaks are slightly blue shifted for the Co/BP, Fe/BP, and Co-Fe/BP catalysts. This is due to the vibration inhibition from the interfacial interaction between BP and Co (Fe) species. This result is in line with that obtained from the XPS analysis of these catalysts.

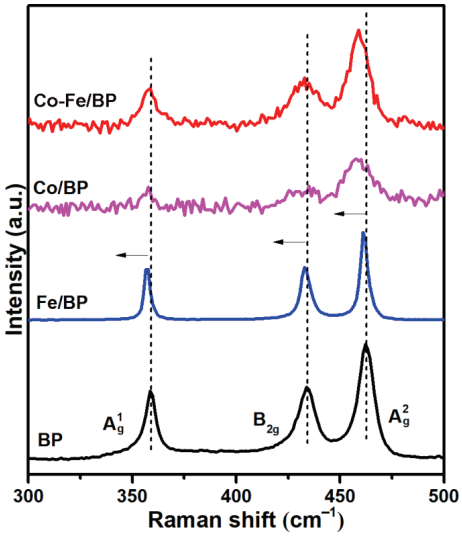

Figure 3 Raman spectra of BP NSs, Co/BP, Fe/BP, and Co-Fe/BP.

The morphologies of these catalysts were further examined by means of SEM. In the SEM image of BP NSs (Fig. S2 in the ESM), small nanosheets are seen. With the introduction of Co or Fe, small nanoparticles are found to be formed on the surface of BP NSs. When both Co and Fe are loaded on BP NSs, more and larger nanoparticles are generated.

The details of the Co-Fe/BP heterostructure were uncovered by means of TEM, high-resolution transmission electron microscopy (HRTEM), and scanning transmission electron microscopy (STEM). From one representative TEM image of the Co-Fe/BP (Fig. 4(a)), one can see that the Co-Fe/BP adequately retains the typical lamellar structure of the BP NSs. In addition, due to thermal effect of the solvothermal treatment, these obtained large nanosheets via electrochemical exfoliation are broken into small nanosheets and are stacked, thus small irregular aggregates are visible on the surface of the BP NSs.

The representative HRTEM images (Figs. 2(b) and 2(c)) of the Co-Fe/BP heterojunction suggest CoFe oxides were successfully loaded on BP NSs. Noticeably, a lattice fringe spacing of 0.28 nm well matches with the (220) of Co_3O_4 (Fig. 2(b)), indicating the presence of Co species on the Co-Fe/BP heterostructure. Additionally, Fe species are also loaded over the Co-Fe/BP heterostructure, as inferred from the observed lattice fringe spacings of 0.19 nm since they are indexed to the (411) plane of Fe_2O_3. These HRTEM images also verify the formed interface between CoO_x and Fe_2O_3, consistent with XPS results. The formed O bridge via the interface could effectively promote electron transfer. Meanwhile, an interplanar distance of 0.22 nm corresponding to the (002) plane of BP is also observed. The corresponding elemental mapping images of P (Fig. 4(e)), Co (Fig. 4(f)), Fe (Fig. 4(g)), and O (Fig. 4(h)) suggest their uniform distribution, proving the formation of uniform CoFe oxides over the BP NSs in the Co-Fe/BP catalyst. Observed lattice fringes corresponding to Co_3O_4 and Fe_2O_3 illustrate the crystalline feature of Co or Fe oxides. But characteristic peaks of Co_3O_4 and Fe_2O_3 over Co-Fe/BP in XRD spectra are not observed. This phenomenon can be explained from two aspects: For one thing, the formed Co_3O_4 and Fe_2O_3 over Co-Fe/BP are impure,

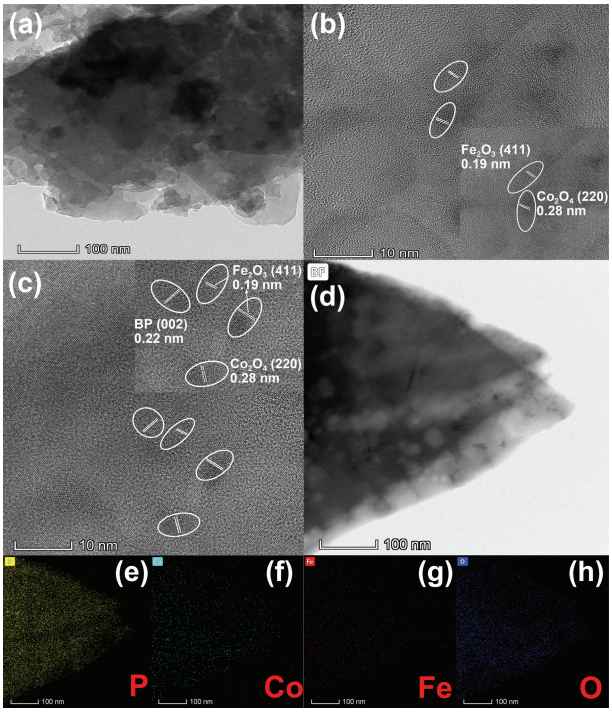

Figure 4 (a) TEM image, (b) and (c) HRTEM images, (d) HAADF-STEM image, and (e)–(h) corresponding EDS mapping images of Co-Fe/BP.

amorphous phase components are mixed or doped with crystalline Co_3O_4 and Fe_2O_3. This makes the formed Co_3O_4 and Fe_2O_3 exhibit extremely low crystallinity; for the other, as is known, the smaller the particles is, the wider the peaks in XRD spectra will be. Because the doped Co_3O_4 and/or Fe_2O_3 species over BP in Co-Fe/BP are very small, thin, and irregular, leading to the widening of peaks in XRD spectra. That is why peaks corresponding to Co_3O_4 and Fe_2O_3 in XRD are not observed.

3.2 The OER performance of Co-Fe/BP

The electrocatalytic OER activities of these obtained catalysts were examined in 1 M KOH by means of linear sweep voltammetry. Considering the semiconductor properties of BP NSs and iron oxide, the LSVs were recorded before and after the application of light illumination (Fig. 5(a)). The corresponding overpotential values at a current density of 10 mA·cm^{-2} for these catalysts were compared (Fig. 5(b)), where no *iR*-compensation was applied.

Without the application of light illumination, the overpotentials of these catalysts follow the order of Co-Fe/BP (290 mV) < Co/BP (387 mV) < BP (460 mV) < Fe/BP (620 mV). The activity of BP NSs substrate is lower than that of Co species, but higher than that of Fe species. This fact indicates that the interaction between Fe and Co species improves the activity of the catalyst, rather than the interaction between Fe species and BP NSs. Moreover, the Co species shows higher OER activity than Fe species, probably due to a poor conductivity of Fe species [31].

When the light illumination is applied, all the OER activities of these catalysts are improved (Δ is defined as the difference value between the overpotentials of obtained catalyst with or without light): ΔCo-Fe/BP = 10 mV, ΔCo/BP = 17 mV, ΔBP = 30 mV, and ΔFe/BP = 120 mV. Especially, the Fe/BP catalyst shows greater improvement in its OER activity than the Co/BP catalyst, perhaps benefiting from its favorable bandgap structure [32–34]. The overpotential order of these catalysts obtained under light illumination: Co-Fe/BP (280 mV) < Co/BP (370 mV) < BP (430 mV) < Fe/BP (500 mV) is exactly same as that obtained without light illumination. Therefore, the transition Co species still show superior OER activity to Fe species and BP NSs, despite of the promotion of light illumination on Fe species and BP NSs. The OER performance of the Co-Fe/BP catalyst is even comparable to other recently reported Co, Fe-based electrocatalysts (Table S2 in the ESM) [22, 25, 35–42]. OER performance of the control sample obtained by physical mixing of BP NSs and metal oxides was tested to compare with that of Co-Fe/BP. Mixed Co-Fe/BP samples are prepared by combining the CoFe oxides (prepared by electrolysis method) with obtained BP nanosheets based on the ratio over Co-Fe/BP tested by ICP-OES. Then the OER performances of mixed Co-Fe/BP samples were tested. As seen in Fig. S3 in the ESM, with or without introduction of light illumination, the overpotentials over as-prepared Co-Fe/BP are much lower than those over mixed Co-Fe/BP, indicating the Co-Fe/BP shows superior OER performance to the mixture sample.

In order to eliminate the photothermal effect on OER performance with light illumination, a comparable experiment of thermal treatment with 40 °C was carried out. The results confirmed the photothermal effect did not play the role in our experiment (Fig. S4 in the ESM).

Tafel slope analysis was applied to provide insight of the reaction mechanism of our system, especially to clarify the rate-determining step. In alkaline solution, the OER mechanism is generally started with electron transfer on the metal sites and then experiences consecutive reaction steps for conversion of OH^- to O_2 [43, 44]. In the consecutive reaction, a smaller Tafel slope suggests that the rate-determining step is at the ending part of the multiple-electron transfer reaction. It is also the evidence of a superior electrocatalyst. In our case (Fig. 5(c)), the Tafel slopes of BP NSs as well as the Fe/BP, Co/BP, and Co-Fe/BP catalysts are 164.5, 253, 144, and 46 mV dec^{-1}, respectively. It is obvious that the rate-determining step for these catalysts transforms from an electron transfer process to an electron–proton reaction. The composition effect of the Co-Fe/BP catalyst significantly improves the OER performance. Noticeably, with the application of light illumination, the Tafel slopes of these catalysts decrease greatly. They are 41.9, 121, 27, and 2.7 for BP NSs as well as the Fe/BP, Co/BP, and Co-Fe/BP catalysts, respectively. In this regard, light illumination significantly promotes the electron transfer rate of the OER. This was further verified by EIS experiments. For example, the electron transfer rates of these catalysts follow a sequence of Co-Fe/BP > Co/BP > BP > Fe/BP (Fig. 5(d)), namely a smaller diameter of a Nyquist plot. This tendency implies the fastest electron transfer rate of the Co-Fe/BP electrocatalyst toward the OER. This is due to the composition effect among Co species, Fe species, and BP NSs. Moreover, the electron transfer rate of the Co-Fe/BP electrocatalyst is promoted by light illumination.

Electrochemical active surface areas (ECSAs) of these catalysts were further estimated by use of their double-layer capacitance (C_{dl}). Their C_{dl} values (Fig. 5(e)) were calculated from the charged current densities within a potential range of where only non-Faradaic processes occur (Fig. S5 in the ESM). The C_{dl} value of the Co-Fe/BP catalyst is 4.56 mF·cm^{-2}, higher than those of BP NSs as well as the Co/BP and Fe/BP catalysts. Therefore, the Co-Fe/BP catalyst has a larger ECSA and more active sites than other catalysts. The largest ECSA over Co-Fe/BP is attributed to the synergistic effect between Co-Fe oxides and BP supporter.

Long-term stability of the Co-Fe/BP catalyst toward the OER was tested by means of chronoamperometry (Fig. 5(f)). A negligible decay of the current density is seen even after 6 h test, indicating high stability of this catalyst. For comparison, the electrocatalytic OER stability of Co-Fe/BP catalyst under light illumination is also tested, and it also shows a good stability (Fig. S6 in the ESM). Structure of Co-Fe/BP after chronoamperometry measurement is revealed by XPS techniques (Fig. S7 in the ESM). From Co 2p XPS spectra and Fe 2p XPS spectra, it is observed that

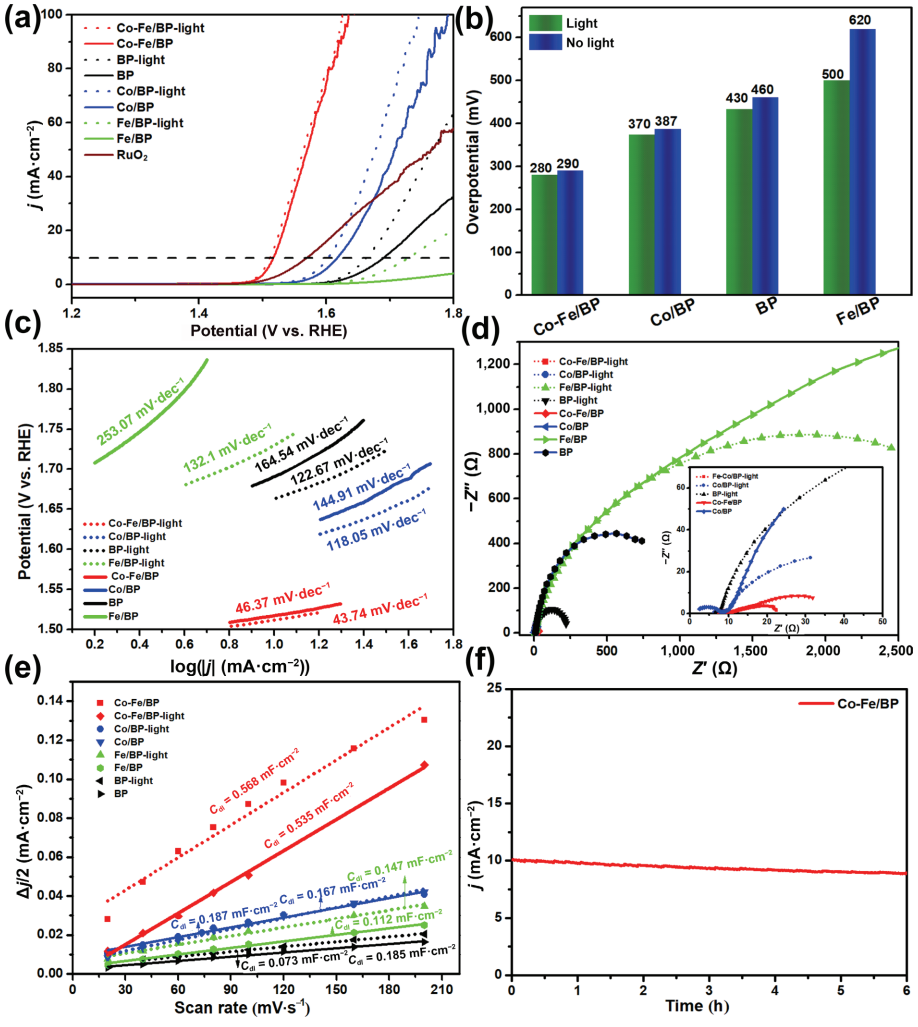

Figure 5 (a) LSVs, (b) overpotential comparison, (c) Tafel plots, (d) Nyquist plots, and (e) C_{dl} values of BP NSs as well as the Co-Fe/BP, Co/BP, and Fe/BP catalysts. (f) Chronoamperometric curve of the Co-Fe/BP catalyst at a constant potential of 1.52 V.

Co and Fe species remains the original oxidation valences after OER, indicating the good stability of this obtained Co-Fe/BP. Furthermore, the intrinsic activity was further investigated by estimating the turnover frequency (TOF) of this catalyst (Table S1 in the ESM) [45]. The Co-Fe/BP exhibited the highest TOF value of 1.70 s^{-1} at 1.60 V (vs. RHE) compared to the Co/BP (0.27 s^{-1}) and Fe/BP (0.015 s^{-1}) catalysts. Consequently, a synergistic effect exists between Co and Fe components in the Co-Fe/BP catalyst. In addition, in order to reveal the influence of electrolytic time on the OER activity, the OER was conducted for different electrolytic times (e.g., 2, 4, and 6 h). The Co-Fe/BP catalyst with an electrolytic time of 4 h showed the best OER performance (e.g., the lowest overpotential of 280 mV) (Fig. S8 in the ESM).

3.3 Photoresponse and adsorption performance of OH* for the Co-Fe/BP catalyst

As demonstrated, light illumination improves the OER performance of these catalysts, especially for BP NSs and the Fe/BP catalyst. To unveil this phenomenon, ultraviolet–visible (UV–vis) diffuse reflectance spectra of these catalysts were recorded (Fig. 6(a)). Accordingly, their optical band gap energies (E_g) were calculated (Fig. S9 in the ESM) on base of the dependence of the absorption coefficient on the photon energy in these absorption spectra (190–1,100 nm) [33]. The E_g values of BP NSs and the Fe/BP catalyst are lower than those of the Co-Fe/BP and Co/BP catalysts. In this context, smaller band gap values lead to superior photoresponse of BP NPs and the Fe/BP catalyst. To further investigate the photoresponse of these catalysts, specific curves of chopped transient photocurrent density vs. illumination time were analyzed in accompany with the period of light on/off every 100 s under light irradiation. These catalysts based photoanodes exhibit a fast increase in photocurrent with light-on, while they quickly go back to about zero accompanied by the light-off (Fig. 6(b)). Therefore, the carrier transport from the as-prepared photoanodes is quite fast. Among them, the photocurrent densities of BP NSs and the Fe/BP catalyst are much higher than those of the Co-Fe/BP and Co/BP catalysts, further indicating the superior photoresponse and higher separation efficiencies of the photogenerated carriers for BP NSs and the Fe/BP catalyst.

To further explain excellent OER performance of the Co-Fe/BP heterostructure, the adsorption performance of these obtained catalysts for OER intermediates which are compactly associated with the OER kinetics was investigated. It has been widely accepted that OH* is a very important intermediate in the OER process. Its bonding strength is correlated with bonding strength of subsequently formed oxygen intermediates (e.g., O* and OOH*). Therefore, obtaining a desired OER catalyst with a favorable bonding strength of OH* is very important. The adsorption strength of OH* can be detected using methanol oxidation reaction (MOR) under identified working conditions for an OER process. Here, OH* species are electrophiles and they can be detected by nucleophiles such as methanol molecules [25, 46–48]. Our tests of MOR and OER on these catalysts were performed in 1 M KOH solution with and without 1 M methanol. The degree of surface OH* coverage can be reflected in the form

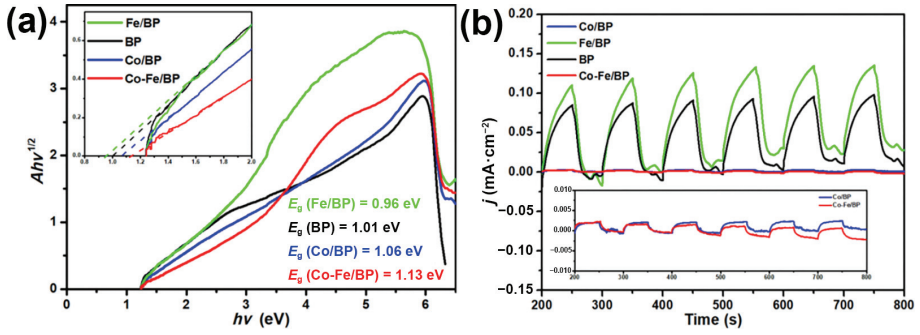

Figure 6 (a) Indirect inter-band transition energy of BP NSs as well as the Co/BP, Fe/BP, and Co-Fe/BP catalysts. (b) Transient photocurrents of BP NSs as well as the Co/BP, Fe/BP, and Co-Fe/BP catalysts in 1 M KOH solution under illumination on a normal timescale.

of the current difference that is resulted from MOR and OER. The current difference (filled area) for these catalysts is in the order of (Fig. 7): $S_{Co\text{-}Fe/BP}$ (0.83) > $S_{Co/BP}$ (0.44) > S_{BP} (0.076) > $S_{Fe/BP}$ (0.0034), demonstrating that the adsorption strength toward OH* varies in the trend: Co-Fe/BP > Co/BP > BP > Fe/BP. More interestingly, the introduction of Fe to BP weakens the OH* adsorption, while the introduction of Co to BP strengthens the OH* adsorption. The Co-Fe/BP catalyst exhibits the strongest adsorption of OH*. This improved catalytic performance of the Co-Fe/BP catalyst originates from the favorable bonding strength of the O intermediate.

3.4 Structure-activity for Co-Fe/BP

The superior OER performance of the Co-Fe/BP catalyst is assumed to be originated from the following aspects (Fig. 8(a)). Formed O bridge via the interface between Co oxides and Fe oxides promotes the electron migration from Fe to Co, which could effectively adjust the electronic structure of CoFe oxides. Moreover, coupling BP NSs with cobalt-iron oxide further moderates the adsorption of oxygen-containing intermediates to an optimal status for a promoted OER process, which enhances electrochemical behavior of Co-Fe/BP. In addition, the combination of cobalt-iron oxide and BP NSs provides many active sites for the OER. Co-O-Fe species over Co-Fe/BP serve as the main active sites species, and the electron migration from Fe to Co along the O bridge via the interface could efficiently improve intrinsic activity for OER, while edge P sites in BP NSs could also serve as active sites. This enlarged ECSA also ensures the excellent OER performance. Furthermore, BP NSs have a high carrier mobility and can serve as the charge transport medium to greatly improve charge conduction, again leading to enhanced OER activity. Interestingly, with favorable band gap structures and superior photoresponse, both BP NSs and iron oxide deliver a photoelectrocatalytic path for the OER. With the introduction of light illumination, photogenerated carriers (holes) over the Co-Fe/BP heteostructure provide new additional active centers for the OER, which further enhances its OER performance (Fig. 8(b)).

4 Conclusions

In summary, an electrochemical method with three-electrode system (a single cathode and double anodes) has been designed to synthesize a cobalt-iron oxide/BP NSs heterostructure. This heterostructure shows a lower overpotential toward the OER than the RuO_2 catalyst, on account of its favorable adsorption behavior and superior ECSA. The synergistic effect among Co, Fe, and BP NSs enhances its OER activity. For example, coupling cobalt-iron oxide with BP NSs regulates the adsorption of oxygen-containing intermediates to a favorable status for an enhanced OER process, as confirmed by the MOR test under the identified operating

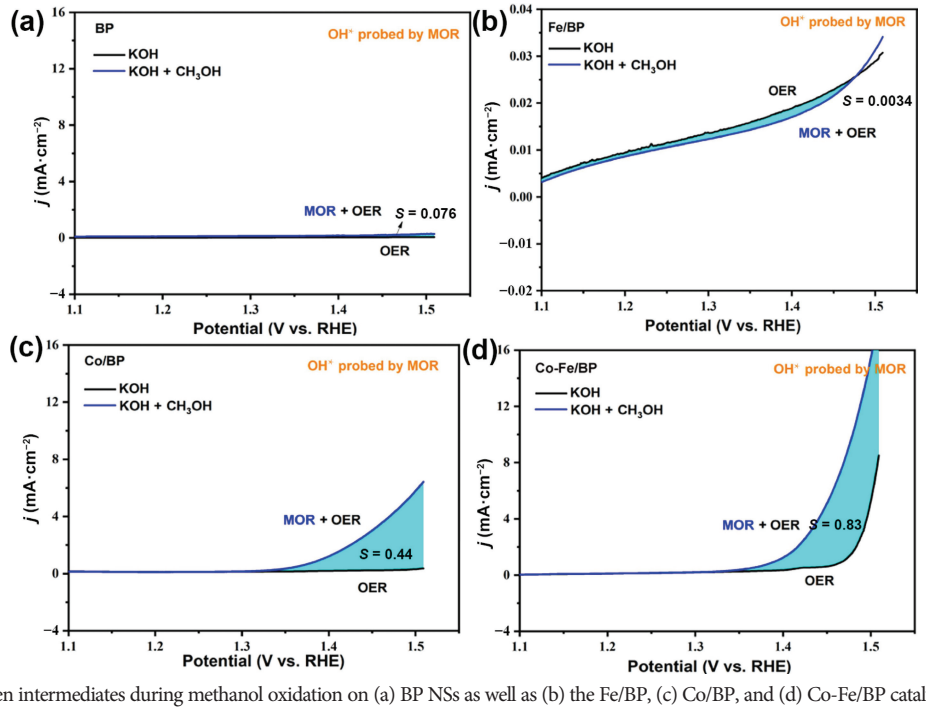

Figure 7 LSVs of oxygen intermediates during methanol oxidation on (a) BP NSs as well as (b) the Fe/BP, (c) Co/BP, and (d) Co-Fe/BP catalysts in 1 M KOH (black) and 1 M KOH + CH_3OH (purple) at a scan rate of 50 mV·s^{-1}. These filled areas are the current difference that is caused by MOR.

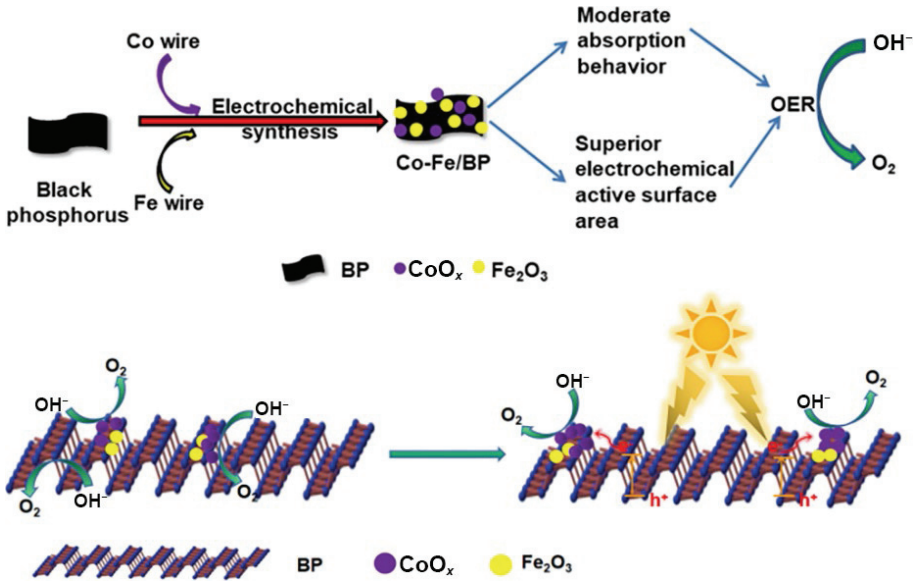

Figure 8 Schematic illustration of (a) composition effect and (b) light illumination of the Co-Fe/BP catalyst for the promoted OER.

conditions of the OER. The combination of cobalt-iron oxide and BP NSs offers the active sites for OER, which in turn contributes to superior ECSAs for excellent OER performance. When the light illumination is applied to the Co-Fe/BP catalyst with a favorable band gap, its OER activity is further improved. This is attributed to an additional photoelectrocatalytic path that is originated from photogenerated carriers (holes) over the Co-Fe/BP heterostructure. This study paves a new way to design, synthesize, and employ photochemically and electrochemically active OER catalysts.

Acknowledgements

This research was supported by the National Natural Science Foundation of China (No. 21571119), the Applied Basic Research Project of Shanxi Province (Nos. 201901D211393 and 201901D211398), Scientific and Technological Innovation Programs of Higher Education Institution in Shanxi (No. 2019L0466), the Graduate Education Innovation Project of Shanxi Province (No. 2021Y480), the Graduate Education Innovation Project of Shanxi Normal University (No. 2021XSY038), and 1331 Engineering of Shanxi Province.

Funding note: Open Access funding enabled and organized by Projekt DEAL.

Electronic Supplementary Material: Supplementary material (SEM images, CV curves, LSV curves and UV–vis absorption spectra of the BP, Co/BP, Fe/BP, and Co-Fe/BP) is available in the online version of this article at https://doi.org/10.1007/s12274-022-4676-9.

References

[1] Xu, W. J.; Cao, D. F.; Moses, O. A.; Sheng, B. B.; Wu, C. Q.; Shou, H. W.; Wu, X. J.; Chen, S. M.; Song, L. Probing self-optimization of carbon support in oxygen evolution reaction. *Nano Res.* **2021**, *14*, 4534–4540.

[2] Wang, T. J.; Liu, X. Y.; Li, Y.; Li, F. M.; Deng, Z. W.; Chen, Y. Ultrasonication-assisted and gram-scale synthesis of Co-LDH nanosheet aggregates for oxygen evolution reaction. *Nano Res.* **2020**, *13*, 79–85.

[3] Sharma, L.; Katiyar, N. K.; Parui, A.; Das, R.; Kumar, R.; Tiwary, C. S.; Singh, A. K.; Halder, A.; Biswas, K. Low-cost high entropy alloy (HEA) for high-efficiency oxygen evolution reaction (OER). *Nano Res.* **2022**, *15*, 4799–4806.

[4] Wu, X. X.; Zhang, T.; Wei, J. X.; Feng, P. F.; Yan, X. B.; Tang, Y. Facile synthesis of Co and Ce dual-doped Ni_3S_2 nanosheets on Ni foam for enhanced oxygen evolution reaction. *Nano Res.* **2020**, *13*, 2130–2135.

[5] Zhao, M.; Xue, S. F.; Xiao, H.; Gao, J. R.; Cheng, X. R.; Jing, Y. Y.; Jia, J. F.; Wu, H. S. Facile *in-situ* electrochemical fabrication of highly efficient nickel hydroxide-iron hydroxide/graphene hybrid for oxygen evolution reaction. *Int. J. Hydrogen Energy* **2022**, *47*, 12547–12558.

[6] Li, M.; Pan, X. C.; Jiang, M. Q.; Zhang, Y. F.; Tang, Y. W.; Fu, G. T. Interface engineering of oxygen-vacancy-rich CoP/CeO_2 heterostructure boosts oxygen evolution reaction. *Chem. Eng. J.* **2020**, *395*, 125160.

[7] Song, J. J.; Wei, C.; Huang, Z. F.; Liu, C. T.; Zeng, L.; Wang, X.; Xu, Z. J. A review on fundamentals for designing oxygen evolution electrocatalysts. *Chem. Soc. Rev.* **2020**, *49*, 2196–2214.

[8] Shi, Z. P.; Wang, X.; Ge, J. J.; Liu, C. P.; Xing, W. Fundamental understanding of the acidic oxygen evolution reaction: Mechanism study and state-of-the-art catalysts. *Nanoscale* **2020**, *12*, 13249–13275.

[9] Zhao, M.; Zhang, J. J.; Xiao, H.; Hu, T. J.; Jia, J. F.; Wu, H. S. Facile *in situ* synthesis of a carbon quantum dot/graphene heterostructure as an efficient metal-free electrocatalyst for overall water splitting. *Chem. Commun.* **2019**, *55*, 1635–1638.

[10] Geng, J.; Kuai, L.; Kan, E. J.; Wang, Q.; Geng, B. Y. Precious-metal-free Co-Fe-O/RGO synergetic electrocatalysts for oxygen evolution reaction by a facile hydrothermal route. *ChemSusChem* **2015**, *8*, 659–664.

[11] Smith, R. D. L.; Prévot, M. S.; Fagan, R. D.; Zhang, Z. P.; Sedach,

P. A.; Siu, M. K. J.; Trudel, S.; Berlinguette, C. P. Photochemical route for accessing amorphous metal oxide materials for water oxidation catalysis. *Science* **2013**, *340*, 60–63.

[12] Yan, M. L.; Zhao, Z. Y.; Cui, P. X.; Mao, K.; Chen, C.; Wang, X. Z.; Wu, Q.; Yang, H.; Yang, L. J.; Hu, Z. Construction of hierarchical $FeNi_3$@(Fe, Ni)S_2 core-shell heterojunctions for advanced oxygen evolution. *Nano Res.* **2021**, *14*, 4220–4226.

[13] Huang, L. A.; He, Z. S.; Guo, J. F.; Pei, S. E.; Shao, H. B.; Wang, J. M. Photodeposition fabrication of hierarchical layered Co-doped Ni oxyhydroxide ($Ni_xCo_{1-x}OOH$) catalysts with enhanced electrocatalytic performance for oxygen evolution reaction. *Nano Res.* **2020**, *13*, 246–254.

[14] Yin, P. Q.; Wu, G.; Wang, X. Q.; Liu, S. J.; Zhou, F. Y.; Dai, L.; Wang, X.; Yang, B.; Yu, Z. Q. NiCo-LDH nanosheets strongly coupled with GO-CNTs as a hybrid electrocatalyst for oxygen evolution reaction. *Nano Res.* **2021**, *14*, 4783–4788.

[15] Smith, R. D. L.; Prévot, M. S.; Fagan, R. D.; Trudel, S.; Berlinguette, C. P. Water oxidation catalysis: Electrocatalytic response to metal stoichiometry in amorphous metal oxide films containing iron, cobalt, and nickel. *J. Am. Chem. Soc.* **2013**, *135*, 11580–11586.

[16] Xiao, H.; Du, X. L.; Zhao, M.; Li, Y.; Hu, T. J.; Wu, H. S.; Jia, J. F.; Yang, N. J. Structural dependence of electrosynthesized cobalt phosphide/black phosphorus pre-catalyst for oxygen evolution in alkaline media. *Nanoscale* **2021**, *13*, 7381–7388.

[17] Xiao, H.; Zhao, M.; Zhang, J. J.; Ma, X. F.; Zhang, J.; Hu, T. J.; Tang, T.; Jia, J. F.; Wu, H. S. Electrochemical cathode exfoliation of bulky black phosphorus into few-layer phosphorene nanosheets. *Electrochem. Commun.* **2018**, *89*, 10–13.

[18] Li, S. T.; Zhang, Y. H.; Huang, H. W. Black phosphorus-based heterostructures for photocatalysis and photoelectrochemical water splitting. *J. Energy Chem.* **2022**, *67*, 745–779.

[19] Xu, Y. M.; Zhang, X. Q.; Chen, Z. H.; Kempa, K.; Wang, X.; Shui, L. L. Chemical vapor deposition of amorphous molybdenum sulphide on black phosphorus for photoelectrochemical water splitting. *J. Mater. Sci. Technol.* **2021**, *68*, 1–7.

[20] Jiang, Q. Q.; Xu, L.; Chen, N.; Zhang, H.; Dai, L. M.; Wang, S. Y. Facile synthesis of black phosphorus: An efficient electrocatalyst for the oxygen evolving reaction. *Angew. Chem., Int. Ed.* **2016**, *55*, 13849–13853.

[21] Nakhanivej, P.; Yu, X.; Park, S. K.; Kim, S.; Hong, J. Y.; Kim, H. J.; Lee, W.; Hwang, J. Y.; Yang, J. E.; Wolverton, C. et al. Revealing molecular-level surface redox sites of controllably oxidized black phosphorus nanosheets. *Nat. Mater.* **2019**, *18*, 156–162.

[22] Li, X. Y.; Xiao, L. P.; Zhou, L.; Xu, Q. C.; Weng, J.; Xu, J.; Liu, B. Adaptive bifunctional electrocatalyst of amorphous CoFe oxide @ 2D black phosphorus for overall water splitting. *Angew. Chem., Int. Ed.* **2020**, *59*, 21106–21113.

[23] Shi, F. B.; Huang, K. K.; Wang, Y.; Zhang, W.; Li, L. P.; Wang, X. Y.; Feng, S. H. Black phosphorus-modified Co_3O_4 through tuning the electronic structure for enhanced oxygen evolution reaction. *ACS Appl. Mater. Interfaces* **2019**, *11*, 17459–17466.

[24] Wang, J. H.; Liu, D. N.; Huang, H.; Yang, N.; Yu, B.; Wen, M.; Wang, X.; Chu, P. K.; Yu, X. F. In-plane black phosphorus/dicobalt phosphide heterostructure for efficient electrocatalysis. *Angew. Chem., Int. Ed.* **2018**, *57*, 2600–2604.

[25] Chen, H. Y.; Chen, J. X.; Ning, P.; Chen, X.; Liang, J. H.; Yao, X.; Chen, D.; Qin, L. S.; Huang, Y. X.; Wen, Z. H. 2D heterostructure of amorphous CoFeB coating black phosphorus nanosheets with optimal oxygen intermediate absorption for improved electrocatalytic water oxidation. *ACS Nano* **2021**, *15*, 12418–12428.

[26] Xiao, H.; Xue, S. F.; Zhang, J. J.; Zhao, M.; Ma, J. C.; Chen, S.; Zheng, Z. F.; Jia, J. F.; Wu, H. S. Facile electrolytic synthesis of Pt and carbon quantum dots coloaded multiwall carbon nanotube as highly efficient electrocatalyst for hydrogen evolution and ethanol oxidation. *Chem. Eng. J.* **2021**, *408*, 127271.

[27] Xiao, H.; Zhang, J. J.; Zhao, M.; Ma, J. C.; Li, Y.; Hu, T. J.; Zheng, Z. F.; Jia, J. F.; Wu, H. S. Electric field-assisted synthesis of Pt, carbon quantum dots-coloaded graphene hybrid for hydrogen evolution reaction. *J. Power Sources* **2020**, *451*, 227770.

[28] Nsanzimana, J. M. V.; Gong, L. Q.; Dangol, R.; Reddu, V.; Jose, V.; Xia, B. Y.; Yan, Q. Y.; Lee, J. M.; Wang, X. Tailoring of metal boride morphology via anion for efficient water oxidation. *Adv. Energy Mater.* **2019**, *9*, 1901503.

[29] Burke, M. S.; Kast, M. G.; Trotochaud, L.; Smith, A. M.; Boettcher, S. W. Cobalt-iron (oxy)hydroxide oxygen evolution electrocatalysts: The role of structure and composition on activity, stability, and mechanism. *J. Am. Chem. Soc.* **2015**, *137*, 3638–3648.

[30] Babar, P.; Patil, K.; Karade, V.; Gour, K.; Lokhande, A.; Pawar, S.; Kim, J. H. *In situ* fabrication of nickel-iron oxalate catalysts for electrochemical water oxidation at high current densities. *ACS Appl. Mater. Interfaces* **2021**, *13*, 52620–52628.

[31] Xu, J. Y.; Li, J. J.; Xiong, D. H.; Zhang, B. S.; Liu, Y. F.; Wu, K. H.; Amorim, I.; Li, W.; Liu, L. F. Trends in activity for the oxygen evolution reaction on transition metal (M = Fe, Co, Ni) phosphide pre-catalysts. *Chem. Sci.* **2018**, *9*, 3470–3476.

[32] Tian, B.; Tian, B. N.; Smith, B.; Scott, M. C.; Hua, R. N.; Lei, Q.; Tian, Y. Supported black phosphorus nanosheets as hydrogen-evolving photocatalyst achieving 5.4% energy conversion efficiency at 353 K. *Nat. Commun* **2018**, *9*, 1397.

[33] Tatlıdil, İ.; Bacaksız, E.; Buruk, C. K.; Breen, C.; Sökmen, M. A short literature survey on iron and cobalt ion doped TiO_2 thin films and photocatalytic activity of these films against fungi. *J. Alloys Compd.* **2012**, *517*, 80–86.

[34] Asif, S. A. B.; Khan, S. B.; Asiri, A. M. Efficient solar photocatalyst based on cobalt oxide/iron oxide composite nanofibers for the detoxification of organic pollutants. *Nanoscale Res. Lett.* **2014**, *9*, 510.

[35] Li, J. C.; Zhou, Q. W.; Zhong, C. L.; Li, S. W.; Shen, Z. H.; Pu, J.; Liu, J. Y.; Zhou, Y. N.; Zhang, H. G.; Ma, H. X. $(Co/Fe)_4O_4$ cubane-containing nanorings fabricated by phosphorylating cobalt ferrite for highly efficient oxygen evolution reaction. *ACS Catal.* **2019**, *9*, 3878–3887.

[36] Wen, T.; Zheng, Y.; Zhang, J.; Davey, K.; Qiao, S. Z. Co(II) boron imidazolate framework with rigid auxiliary linkers for stable electrocatalytic oxygen evolution reaction. *Adv. Sci.* **2019**, *6*, 1801920.

[37] Chen, H. Y.; Song, L. Z.; Ouyang, S. X.; Wang, J. B.; Lv, J.; Ye, J. H. Co and Fe codoped $WO_{2.72}$ as alkaline-solution-available oxygen evolution reaction catalyst to construct photovoltaic water splitting system with solar-to-hydrogen efficiency of 16.9%. *Adv. Sci.* **2019**, *6*, 1900465.

[38] Shi, J. H.; Qiu, F.; Yuan, W. B.; Guo, M. M.; Lu, Z. H. Nitrogen-doped carbon-decorated yolk-shell CoP@FeCoP micro-polyhedra derived from MOF for efficient overall water splitting. *Chem. Eng. J.* **2021**, *403*, 126312.

[39] Ge, K.; Sun, S. J.; Zhao, Y.; Yang, K.; Wang, S.; Zhang, Z. H.; Cao, J. Y.; Yang, Y. F.; Zhang, Y.; Pan, M. W. et al. Facile synthesis of two-dimensional iron/cobalt metal-organic framework for efficient oxygen evolution electrocatalysis. *Angew. Chem., Int. Ed.* **2021**, *60*, 12097–12102.

[40] Chen, J. S.; Li, H.; Pei, Z. X.; Huang, Q. W.; Yuan, Z. W.; Wang, C. J.; Liao, X. Z.; Henkelman, G.; Chen, Y.; Wei, L. Catalytic activity atlas of ternary Co-Fe-V metal oxides for the oxygen evolution reaction. *J. Mater. Chem. A* **2020**, *8*, 15951–15961.

[41] Zhang, H. B.; Zhou, W.; Dong, J. C.; Lu, X. F.; Lou, X. W. Intramolecular electronic coupling in porous iron cobalt (oxy)phosphide nanoboxes enhances the electrocatalytic activity for oxygen evolution. *Energy Environ. Sci.* **2019**, *12*, 3348–3355.

[42] Guo, C. Y.; Liu, X. J.; Gao, L. F.; Ma, X. J.; Zhao, M. Z.; Zhou, J. Z.; Kuang, X.; Deng, W. Q.; Sun, X.; Wei, Q. Oxygen defect engineering in cobalt iron oxide nanosheets for promoted overall water splitting. *J. Mater. Chem. A* **2019**, *7*, 21704–21710.

[43] Zhang, G. X.; Yang, J.; Wang, H.; Chen, H. B.; Yang, J. L.; Pan, F. $Co_3O_{4-\delta}$ quantum dots As a highly efficient oxygen evolution reaction catalyst for water splitting. *ACS Appl. Mater. Interfaces* **2017**, *9*, 16159–16167.

[44] Zhao, Y.; Nakamura, R.; Kamiya, K.; Nakanishi, S.; Hashimoto, K. Nitrogen-doped carbon nanomaterials as non-metal electrocatalysts for water oxidation. *Nat. Commun.* **2013**, *4*, 2390.

[45] Anantharaj, S.; Ede, S. R.; Karthick, K.; Sam Sankar, S.; Sangeetha, K.; Karthik, P. E.; Kundu, S. Precision and correctness in the

evaluation of electrocatalytic water splitting: Revisiting activity parameters with a critical assessment. *Energy Environ. Sci.* **2018**, *11*, 744–771.

[46] Tao, H. B.; Xu, Y. H.; Huang, X.; Chen, J. Z.; Pei, L. J.; Zhang, J. M.; Chen, J. G.; Liu, B. A general method to probe oxygen evolution intermediates at operating conditions. *Joule* **2019**, *3*, 1498–1509.

[47] Zhong, J. P.; Hou, C.; Li, L.; Waqas, M.; Fan, Y. J.; Shen, X. C.; Chen, W.; Wan, L. Y.; Liao, H. G.; Sun, S. G. A novel strategy for synthesizing Fe, N, and S tridoped graphene-supported Pt nanodendrites toward highly efficient methanol oxidation. *J. Catal.* **2020**, *381*, 275–284.

[48] Zhang, J. M.; Sun, S. N.; Li, Y.; Zhang, X. J.; Zhang, P. Y.; Fan, Y. J. A strategy in deep eutectic solvents for carbon nanotube-supported PtCo nanocatalysts with enhanced performance toward methanol electrooxidation. *Int. J. Hydrogen Energy* **2017**, *42*, 26744–26751.